Numerical Analyses on Plasma Acceleration Processes in Applied-Field Magnetoplasmadynamic Thruster

IEPC-2009-227

Presented at the 31st International Electric Propulsion Conference,
University of Michigan • Ann Arbor, Michigan • USA
September 20 – 24, 2009

K. Kubota[1] and I. Funaki[2]
Japan Aerospace Exploration Agency, Sagamihara, Kanagawa, 229-8510, Japan

and

Y. Okuno[3]
Tokyo Institute of Technology, Yokohama, Kanagawa, 226-8502, Japan

Abstract: The acceleration processes of plasma flows in an applied-field magnetoplasmadynamic thruster are numerically investigated with a physical model including the ion-rich sheath effect on an anode. A heat transfer model regarding the electron energy through the anode is also taken into account. An external magnetic field of 0.1 and 0.15 T is applied to argon propellant of 0.1 g/s under a constant discharge current of 1 kA. Comparing the current contour lines with and without the sheath model, it is shown that the current contour lines calculated with the sheath model tend to shift toward upstream region around the diverging anode surface due to the presence of an anode sheath. Then about 50% of the input power is lost through the anode surface, although the ion-rich sheath decelerating the electrons reduces the net anode heat loss to 15-17% of the input power. It is also shown that an increase in the strength of the applied magnetic field reduces the ratio of the anode heat loss to the input power by virtue of magnetic nozzle effect.

Nomenclature

A	=	Vector potential
$\boldsymbol{B}$	=	Magnetic flux density
e	=	Elementary charge
$\boldsymbol{E}$	=	Electric field
$\bar{I}$	=	Unit Tensor
$\boldsymbol{j}$	=	Current density
J	=	Discharge current
J_c	=	Coil current
k	=	Boltzmann constant
l	=	Mean free path
m_s	=	Mass of species s
M	=	Atomic weight
n	=	Number density
p	=	Pressure
$\boldsymbol{q}$	=	Heat flux

[1] Research Fellow of JSPS, Institute of Space and Astronautical Science, Email: kubota.kenichi@jaxa.jp
[2] Associate Professor, Institute of Space and Astronautical Science, Email: funaki@isas.jaxa.jp
[3] Professor, Tokyo Institute of Technology, Email: yokuno@es.titech.ac.jp

r = Radial coordinate
T = Temperature
U = Internal energy
$\boldsymbol{u}$ = Velocity
V_i = Ionization energy
V_{sh} = Sheath voltage
V_f = Floating voltage
z = Axial coordinate
θ = Azimuthal coordinate
λ = Thermal conductivity
μ = viscosity coefficient
μ_0 = permeability in vacuum
ρ = Mass density
σ = Electrical conductivity
$\bar{\tau}$ = Viscous stress tensor
Φ = Dissipation function

Subscripts

ap = Applied
e = Electron
h = Heavy particle (neutral, ion)
i = ion

I. Introduction

Recently, desirable power range for an electric propulsion device is getting larger in accordance with expanding scales of new and ambitious space missions. A magnetoplasmadynamic thruster (MPDT) is known as a representative high-power electric propulsion device. A suitable power range for an applied-field MPDT (AFMPDT) is considered to be 10 kW – 100 kW which will be promising power range for a high-power electric propulsion device in the next generation,[1] hence development of an efficient AFMPDT is eagerly anticipated.

Figure 1 shows the principle of an AFMPDT. Application of a magnetic field with an external coil surrounding a MPDT yields azimuthal Lorentz force resulting in a swirl flow, and its kinetic energy is converted into an axial kinetic energy via a solid and/or a magnetic nozzle. The acceleration with the magnetic nozzle is attributed to Lorentz force produced by an azimuthally induced current and the radial component of the applied magnetic field, which is generally called Hall acceleration.

There have been many experimental efforts to establish a guideline for high-performance operation.[2] On the other hand, in terms of numerical approaches, Tanaka *et al*. conducted the flowfield analysis in which the two-dimensional equations for the electromagnetic field analysis, and quasi-one dimensional equations for the flowfield are adopted.[3] Thomas *et al*. simulated high power AFMPDT flows with Ar propellant of 20-30 g/s at a discharge current of 3-17.5 kA.[4] Mikellides *et al*. developed a two-dimensional simulation code (MACH2) with a comprehensive physical model for the analyses of the flowfields in the NASA Lewis Research Center 100-kW-classs applied-field MPD thruster, and obtained a good agreement with the experimental results.[5] It was reported that the aerodynamic acceleration is dominant under the condition of Ar propellant of 0.1 g/s, a discharge current of 1 kA, an external magnetic field of 0.1 T. Recently, 10-20 kW class AFMPDT was simulated by Haag with SAMSA code.[6]

To enhance thrust efficiency of AFMPDTs, clarification of the energy conversion processes of the swirl flow will be of great importance. According to the Myers's experimental results,[7] most of the energy of the plasma flows is lost to the anode surface, hence the anode heat loss has to be estimated to discuss the energy conversion processes. In the proceeding numerical efforts,[8] the anode heat loss has been evaluated under an isothermal condition. Actually, however, the balance of

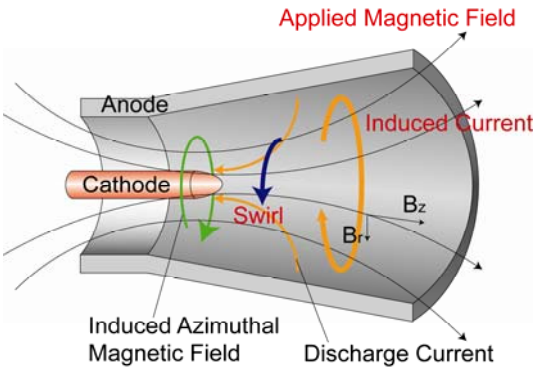

Figure 1. Principle of applied-field MPD thruster.

electron energy on the anode has to be taken into account to determine the electron temperature along the anode, and then we cannot neglect a sheath region between the anode and the plasma. Since the sheath is electrically non-neutral, it is difficult to directly incorporate it in an MHD model, thus uncertainty with regard to the sheath has prevented us from understanding complicated phenomena within an MPD thruster. To treat the sheath effect self-consistently, Roy simulated the self-field MPDT flow with the multi-fluid formulation without assuming electrical neutrality.[9] It was also reported that a large voltage drop near an anode can be simulated even with a quasi-neutral model.[10]

In this study, to investigate the acceleration processes in an AFMPDT in detail, plasma flows are simulated by an MHD model with an anode boundary condition in which a theoretically-modeled anode sheath effect is incorporated. The anode sheath model has been employed to analyze plasma properties in vacuum circuit breakers.[11] With the model, the electron temperature on the anode can be estimated from the electron energy balance relation, which enables us to compute the anode heat loss regarding electrons. The influences of an anode sheath and the anode heat loss on the thrust performances and flowfields of an AFMPDT are quantitatively discussed. Also, the effects of the strength of an applied magnetic field on the energy conversion processes are described.

II. Numerical Model

A. Thruster Geometry

The flow under consideration is assumed to be axisymmetric, and then the computational region can be set as shown in Fig. 2. The thruster consists of a flared anode and a short cathode. Each radius of the anode and the cathode is 14 mm and 4 mm at the inlet where the propellant is injected from a port located at r = 7 – 11 mm. At the outlet (z = 55 mm), the anode is 27 mm in radius, and an insulator is located around the anode. In Fig. 2, the distribution of the applied magnetic field is also depicted. The applied magnetic field is produced by an external coil the properties of which are listed in Table 1. To examine the effect of the strength of magnetic field, the coil current is set at 10, and 15 A, and then the maximum magnetic field is about 0.1, and 0.15 T respectively.

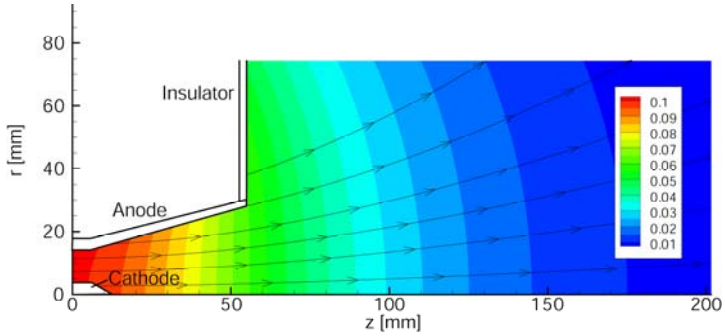

Figure 2. Thruster geometry and distribution of applied magnetic field, T, (J_c = 10 A).

Table 1. Properties of external coil.

Axial position [mm]	-60 ~ 40
Radial position [mm]	40 ~ 140
Layer	40
Windings	40
Coil current (J_c) [A]	10, 15
Maximum Magnetic field (B_{max}) [T]	0.1, 0.15

B. Basic Equations

In this study, argon is used as a propellant, and non-equilibrium singly ionization processes are simulated. The heavy particles (ion, neutral) and the electrons are assumed to be thermally non-equilibrium. The basic equations are conservation equations of mass, momentum, energy (heavy particles, electrons), and the induction equation. The

induction equation is used to determine the azimuthal induced magnetic field. Since the plasma in the AFMPDT rotates due to the azimuthal Lorentz force, we have to take into account the three components of velocity in the formulation. In addition, since the azimuthal induced current will produce axial and radial magnetic fields changing the original applied magnetic field, these components have to be included. In this simulation, the axial and radial magnetic fields are given from an azimuthal vector potential.

$$\frac{\partial \rho}{\partial t} + \nabla \cdot (\rho \boldsymbol{u}) = 0 \tag{1}$$

$$\frac{\partial \rho_i}{\partial t} + \nabla \cdot (\rho_i \boldsymbol{u}) = \dot{\rho}_i \tag{2}$$

$$\frac{\partial \rho \boldsymbol{u}}{\partial t} + \nabla \cdot \left[\rho \boldsymbol{u}\boldsymbol{u} + p\bar{I}\right] = \boldsymbol{j} \times \boldsymbol{B} + \nabla \cdot \bar{\tau} \tag{3}$$

$$\frac{\partial U_h}{\partial t} + \nabla \cdot (U_h \boldsymbol{u}) = -p_h \nabla \cdot \boldsymbol{u} + \Phi - \nabla \cdot \boldsymbol{q}_h + \delta E \tag{4}$$

$$\frac{\partial}{\partial t}(U_e + en_i V_i) + \nabla \cdot [(U_e + en_i V_i)\boldsymbol{u}] = -p_e \nabla \cdot \boldsymbol{u} + \frac{\boldsymbol{j}^2}{\sigma} - \nabla \cdot \boldsymbol{q}_e - \frac{1}{en_e}\boldsymbol{j} \cdot \nabla p_e - \delta E \tag{5}$$

$$\frac{\partial \boldsymbol{B}}{\partial t} - \nabla \times (\boldsymbol{u} \times \boldsymbol{B}) = -\nabla \times \left[\frac{1}{\mu_0 \sigma}\nabla \times \boldsymbol{B} + \frac{1}{\mu_0 en_e}(\nabla \times \boldsymbol{B}) \times \boldsymbol{B} - \frac{1}{en_e}\nabla p_e\right] \tag{6}$$

$$\frac{1}{\mu_0 \sigma}\left(\nabla^2 A_\vartheta - \frac{A_\vartheta}{r^2}\right) + (u_z B_r - u_r B_z) - \frac{1}{en_e}(j_z B_r - j_r B_z) = 0 \tag{7}$$

where

$$B_r = B_{r,ap} - \frac{\partial A_\theta}{\partial z}, \qquad B_z = B_{z,ap} + \frac{1}{r}\frac{\partial r A_\theta}{\partial r} \tag{8}$$

The right hand side of Eq. (2) represents an ion production rate in which it is assumed that ionization is driven only by electron impact. Lotz formula is used as a forward reaction rate,[12] and a backward reaction rate is determined from an equilibrium constant. The internal energies and the ionization energy is defined by

$$U_s = \frac{3}{2} n_s k T_s \tag{9}$$

The δE denotes the rate of energy exchange via elastic collisions between heavy particles and electrons.[13]

$$\delta E = 3 n_e \frac{m_e}{m_h} \nu_{eh} k (T_e - T_h) \tag{10}$$

The heat fluxes can be given as follows.[14]

$$\boldsymbol{q}_h = -\lambda_h \nabla T_h, \quad \boldsymbol{q}_e = -\lambda_e \nabla T_e + \frac{5k}{2e} T_e \boldsymbol{j} \tag{11}$$

The components of the current density are obtained from Ampère's law and generalized Ohm's law.

$$j_r = -\frac{1}{\mu_0 r}\frac{\partial r B_\theta}{\partial z} \tag{12}$$

$$j_\theta = \sigma\left(u_z B_r - u_r B_z - \frac{1}{en_e}(j_z B_r - j_r B_z)\right) \tag{13}$$

$$j_z = \frac{1}{\mu_0 r}\frac{\partial r B_\theta}{\partial r} \tag{14}$$

The viscous coefficient which is required to evaluate the dissipation function Φ is given by[5]

$$\mu = \frac{1}{2}\alpha m_h C_h \sum_{s \neq e} n_s l_s \tag{15}$$

where α is a constant slightly less than unity. The thermal conductivities of the heavy particles and the electrons are calculated from the relations below, where the Prandtl number P_r is assumed to be 2/3 in this study.[13]

$$\lambda_h = \frac{\mu c_p}{P_r}, \qquad \lambda_e = \frac{2.4}{1+\nu_{ei}/\nu_{eh}\sqrt{2}} \frac{k^2 n_e T_e}{m_e \nu_{eh}} \tag{16}$$

The electrical conductivity includes the effect of the anomalous resistivity.[5]

$$\frac{1}{\sigma} = \frac{m_e \nu_{eh}}{e^2 n_e} + \eta_{anm} \tag{17}$$

$$\eta_{anm} = \frac{0.7 m_e}{e\sqrt{\varepsilon_0}} \sqrt{\frac{M}{\rho}} \left(1 - e^{-u_{e,d}/u_{i,ac}}\right) \left(1 + 0.3 \frac{u_{e,d}}{u_{i,ac}} \sqrt{\frac{|\boldsymbol{B}|^2}{|\boldsymbol{B}|^2 + C'\rho/M}}\right) \tag{18}$$

Here, C' is a constant equal to 6.1544×10^7. The $u_{e,d}$ and $u_{i,ac}$ denote the electron drift velocity and the ion acoustic velocity respectively. The collision cross sections are required to evaluate the collision frequencies. We use $Q_{in} = 8 \times 10^{-19}$ m^2,[15] and the following relations.[13,16,17]

$$Q_{si} = \frac{5.85 \times 10^{-10}}{T_s^{\,2}} \ln\left[1.24 \times 10^7 \left(\frac{T_e^{\,3}}{n_e}\right)^{1/2}\right] \qquad \text{(s= i, e)} \tag{19}$$

$$Q_{en} = \frac{2.336 \times 10^{-14}}{C_e} \left(\frac{kT_e}{e}\right)^{1.609} \exp\left[0.0618 \left(\ln \frac{kT_e}{e}\right)^2 - 0.1171 \left(\ln \frac{kT_e}{e}\right)^3\right] \tag{20}$$

$$Q_{nn} = 2.57 \times 10^{-19} \left(1 + \frac{169.9}{T_h}\right) \tag{21}$$

The convective terms in Eq. (1)-(6) are discretized with second-order TVD Lax-Friedrich scheme,[18] and the second-order derivatives are evaluated with the central difference formula. In the time integration, the local time step technique is used to accelerate convergence. Equation (7) is solved with SOR method every several time steps.

C. Boundary Conditions

The mass flow rate, discharge current, and inlet temperature are set at 0.1 g/s, 1 kA, $T_h = 10^3$ K, $T_e = 10^4$ K respectively. Non-slip condition is imposed on the velocity along the walls. The heavy particle temperature T_h on each electrode is limited by the melting temperature point of electrode materials. In this study, T_h is kept to be less than 1,300 K on the anode, and to be less than 2,000 K on the cathode, where the anode and the cathode is assumed to be cupper and Thoriated tungsten respectively. As for the electron temperature, the condition of $\nabla T_e = 0$ is imposed on the cathode. On the other hand, on the anode, the electron temperature T_e is given by a heat loss model, i.e. T_e on the anode is determined by solving the non-linear equation of electron energy balance on the anode surface.[14,19]

$$\boldsymbol{q}_{ent} + \boldsymbol{q}_{conv} - \boldsymbol{q}_{sh} = \boldsymbol{q}_a \tag{22}$$

where

$$\boldsymbol{q}_{ent} = \frac{5k}{2e} T_e j_n \tag{23}$$

$$\boldsymbol{q}_{conv} = -\lambda_e \nabla T_e \tag{24}$$

$$\boldsymbol{q}_{sh} = \frac{1}{4} n_e C_e \exp\left(-\frac{eV_{sh}}{kT_e}\right) eV_{sh} \tag{25}$$

$$\boldsymbol{q}_a = \frac{1}{4} n_e C_e \exp\left(-\frac{eV_{sh}}{kT_e}\right) 2kT_e \tag{26}$$

Here, the j_n denotes the current density normal to the anode surface. $\boldsymbol{q}_{\text{ent}}$, $\boldsymbol{q}_{\text{conv}}$, $\boldsymbol{q}_{\text{sh}}$, and $\boldsymbol{q}_a$ correspond to the diffusion of the electron's enthalpy, convective heat transfer, electron energy lost in the anode sheath, and net heat flux to the anode surface respectively (Fig. 3). In Eqs. (25) and (26), the voltage drop in an anode sheath has to be given. In this study, it is assumed that an ion-rich sheath is formed on the anode surface, since the current density will be less than the electron saturation current j_{th} under the present operating condition.

$$j_{th} = \frac{1}{4} e n_e C_e, \quad C_e = \sqrt{\frac{8kT_e}{\pi m_e}} \tag{27}$$

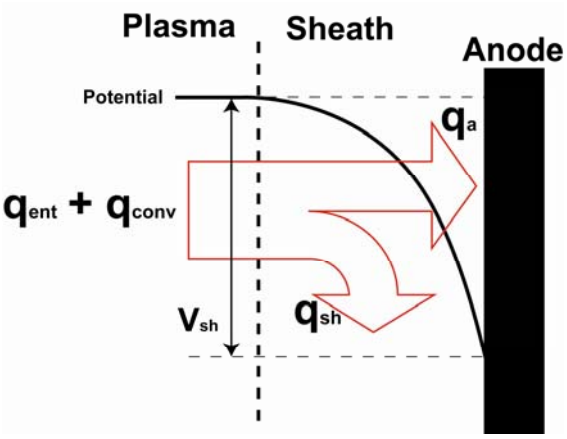

Figure 3. Electron energy balance on anode (An ion-rich sheath is assumed. The sheath voltage V_{sh} is defined so as to be a positive value.).

Then, the anode sheath voltage can be determined by the following relation.

$$V_{sh} = -\frac{kT_e}{e}\ln\left|\frac{j_n}{j_{th}}\right| \tag{28}$$

Here, V_{sh} is defined so as to be a positive value.

Since a collisionless sheath is assumed in the Eq. (22), a mean free path of electrons has to be much larger than the sheath thickness which is often characterized by the Debye length. Given a fully ionized plasma at $T_h = T_e = 4$ eV, $n_e = 10^{21}$ m^{-3}, which is a typical plasma condition within an MPDT, a Debye length and a mean free path of electrons are estimated at 4.7×10^{-7} m and 4.5×10^{-4} m respectively; hence the assumption of a collisionless sheath seems reasonable. In addition, we have to consider the effect of a magnetic field. Under a magnetic field of 0.1 T, a Larmor radius of an electron at 4 eV is about 6.7×10^{-5} m. Since the Larmor radius is much larger than a sheath length, the effect of a magnetic field can be ignored.

The azimuthal induced magnetic field B_θ on the anode is given by the condition that the tangential electric field is equal to the gradient of an anode sheath.[11]

$$E_\xi = -\frac{\partial V_{sh}}{\partial \xi} \tag{29}$$

Here, ξ represents tangential coordinate along the electrodes. By applying the generalized Ohm's law to E_ξ, we can derive an equation to determine B_θ on the anode. For $|j_n/j_{th}| << 1$, the sheath voltage defined in Eq. (28) approaches infinity. In such a case, however, the potential of the anode surface is considered to approach asymptotically to a floating potential V_f, and then the sheath voltage is given by the following equation.

$$V'_{sh} = V_{plasma} - V_f = \frac{kT_e}{e}\ln\left(\frac{2.7m_i}{2\pi m_e}\right)^{1/2} \tag{30}$$

Hence, if V_{sh} given by Eq. (28) is larger than V'_{sh} given by Eq. (30), $V_{sh} = V'_{sh}$ is assumed. On the cathode, we ignore the variation of a sheath along the cathode, i.e. the B_θ on the cathode is determined from the condition of $E_\xi = 0$.

The other components of the induced magnetic fields are calculated by integrating all contributions produced by the azimuthal current in the whole computational domain with Biot-Savart law.

D. Calculation Conditions

The flow is simulated under three calculation conditions (Case1, Case2, Case3) shown in Table 2. Comparing Case1 and Case2, influences of the sheath model and the heat loss model on thrust performance and flowfields can be examined. To clarify the effect of the strength of the applied magnetic field, magnetic field strength is also varied from 0.1 T (Case1, Case2) to 0.15 T (Case3).

Table 2. Calculation conditions.

	B_{max} [T]	Sheath	Boundary Condition of T_e on anode
Case1	0.10	ignored	$\nabla T_e = 0$
Case2	0.10	included	heat loss model of Eq. (22)
Case3	0.15	included	heat loss model of Eq. (22)

III. Numerical Results and Discussion

A. Thrust performance

In order to understand the operating condition under consideration, the thrust performances are shown in Table 3. The thrust F is defined as the sum of the aerodynamic thrust (F_{aero}), electromagnetic thrust regarding self-field (F_{self}), electromagnetic thrust relating with Hall acceleration (F_{Hall}), and the friction loss (F_{vis}). Here, F_{aero} includes the momentum flux at the propellant injection port. Calculating the thrust efficiency, we have to evaluate the sum of an anode sheath and a cathode sheath to estimate a power consumed at a sheath region. Since the cathode sheath is not taken into account in our model, however, we used an assumed constant total sheath voltage as 20 V.

$$\eta = \frac{F^2}{2\dot{m}\left(P_{net} + 20J\right)} \tag{31}$$

where P_{net} denotes a net input energy defined by,

$$P_{net} = \int \boldsymbol{j} \cdot \boldsymbol{E}\, dV \tag{32}$$

Under the present condition, most of the thrust is composed of the aerodynamic thrust. In Case3, each component of the thrust is F_{aero}=1.29 N, F_{self} = 0.13 N, F_{Hall} = 0.16 N, F_{vis} = -0.16 N. In spite of the almost the same P_{net} in Case1 and Case2, the thrust efficiency in Case2 is less than that of Case1 due to the effect of heat loss regarding the electron energy. According to the experimental data of thrust performance obtained by Myers[7] (Ar, 0.1 g/s, J = 1 kA), our numerical results shown in Table 3 seems reasonable, although our thruster geometry differs from them.

Table 3. Thrust performance. Total sheath voltage drop including a cathode sheath is assumed to be 20 V.

	F [N]	I_{sp} [s]	η [%]	P_{net} [kW]
Case1	1.43	1460	17.2	39.2
Case2	1.22	1240	12.2	40.8
Case3	1.42	1450	14.5	52.6

B. Current contour lines

The calculated current contour lines are shown in Fig. 4 for each case. The labeled values on the contour lines denote the ratio of the current flowing downstream viewed from the line to the total discharge current. In Case1, it can be seen that the current contour lines tend to expand toward the downstream region, which is considered to be caused by the Hall effect, i.e. an electron emitted from the cathode is transferred toward downstream region by $\boldsymbol{E} \times \boldsymbol{B}$ drift, and then it is absorbed into the anode. On the other hand, in Case2 and Case3 in which the sheath model is incorporated, we can see that the current contour lines near the anode tend to shift toward upstream region. To clarify the reason for this phenomenon, distribution of the anode sheath voltage is shown in Fig. 5. The result indicates that the anode sheath voltage is gradually decreased in the region of z > 20 mm. As illustrated in Fig. 5, it is supposed that an electric field toward the downstream region is produced in this region, and then an electron comes from upstream region by $\boldsymbol{E} \times \boldsymbol{B}$ drift is pushed back toward upstream region, which results in the current contour lines shown in Fig. 4. The result of the anode sheath voltage ranges from 15 to 25 V (V_{sh} is defined so as to be a positive value). According to the probe diagnosis carried out by Tahara,[20] the voltage of an ion-rich sheath formed under the condition of Ar, 1.37 g/s, J = 5.6 kA is about 20 V. Therefore our numerical result seems reasonable, although our operating condition is different from them.

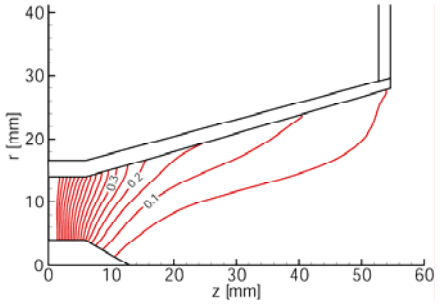

a) Case1 (B_{max}= 0.1 T, w/o sheath model)

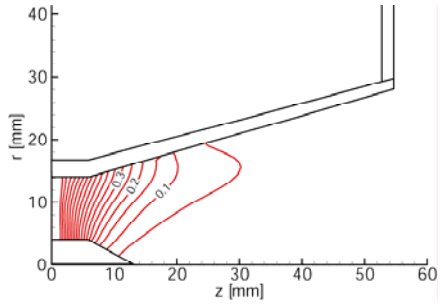

b) Case2 (B_{max}= 0.1 T, with sheath model)

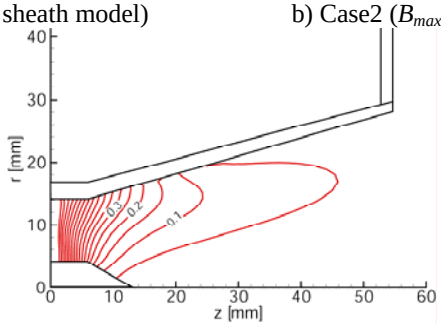

c) Case3 (B_{max}= 0.15 T, with sheath model)

Figure 4. Current contour lines, Ar, 0.1 g/s, J = 1 kA.

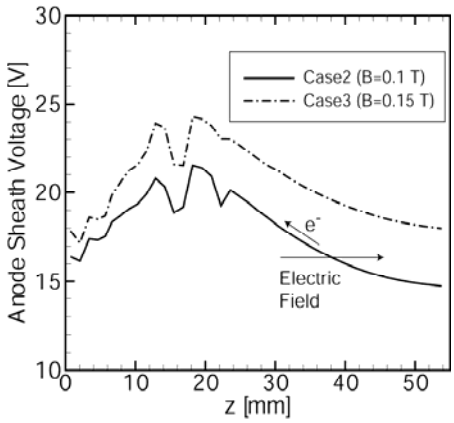

Figure 5. Anode sheath voltage along the anode surface (An ion-rich sheath is assumed. The sheath voltage V_{sh} is defined so as to be a positive value.).

C. Electron temperature

The electron temperature distributions for each case are illustrated in Fig. 6. In Case1, the T_e is about 7 eV around the cathode, and about 6 eV near the anode surface. In Case2, the T_e is decreased in the whole region in comparison with Case1, where the T_e is limited to 4 – 5 eV near the anode surface. From the result of Case3, it can be seen that the T_e is slightly increased by increasing the strength of the applied magnetic field. This fact will be attributed to an increase in the Joule heating resulting from enhanced resistivity caused by the effect of the increased axial magnetic field. Despite the higher magnetic field, the T_e of Case3 is still lower than that of Case1, which suggests a significant heat loss regarding the electron energy.

D. Heat loss on anode

The heat losses of the electron energy on the anode are discussed for Case2 and Case3. We assume that the energy lost from plasma flow (Q_p) consists of the energy loss regarding electron enthalpy (Q_{ent}) and that regarding

convective heat transfer (Q_{conv}). The net heat loss transferred to the anode surface (Q_a) can be obtained by subtracting an energy loss of electrons within the sheath (Q_{sh}) from Q_p.

$$Q_p = \int_{anode} (\boldsymbol{q}_{ent} + \boldsymbol{q}_{conv}) \cdot d\boldsymbol{S} = Q_{ent} + Q_{conv} \tag{33}$$

$$Q_a = Q_p - \int_{anode} \boldsymbol{q}_{sh} \cdot d\boldsymbol{S} = Q_p - Q_{sh} \tag{34}$$

These values are shown in Table 4. In both Case2 and Case3, about 50% of the net input power P_{net} is lost through the anode surface. It can be seen that Q_{conv} is about two times larger than Q_{ent}. Due to the presence of an ion-rich sheath, the electrons lose their energy in the sheath, and then the net energy transferred to the anode Q_a is reduced to 15 – 17% of P_{net}. Assuming that the anode material is cupper, its work function is about 5 eV, which is almost the same as the calculated T_e near the anode. Thus a released energy with regard to electron absorption on the anode is inferred to be the same order as the Q_p or Q_a.

Comparing Case2 with Case3, the heat loss itself for Case3 is higher than that for Case2. This fact will be related with the higher T_e for Case3 due to an increase in Joule heating resulting from raised resistivity by an increased magnetic field. In contrast, the Q_p/P_{net} and Q_a/P_{net} for Case3 are less than those for Case2. Such a tendency of a decrease in the ratio of an anode heat loss to a total input power with increasing an applied magnetic field was also verified in the experiment conducted by Myers.[7]

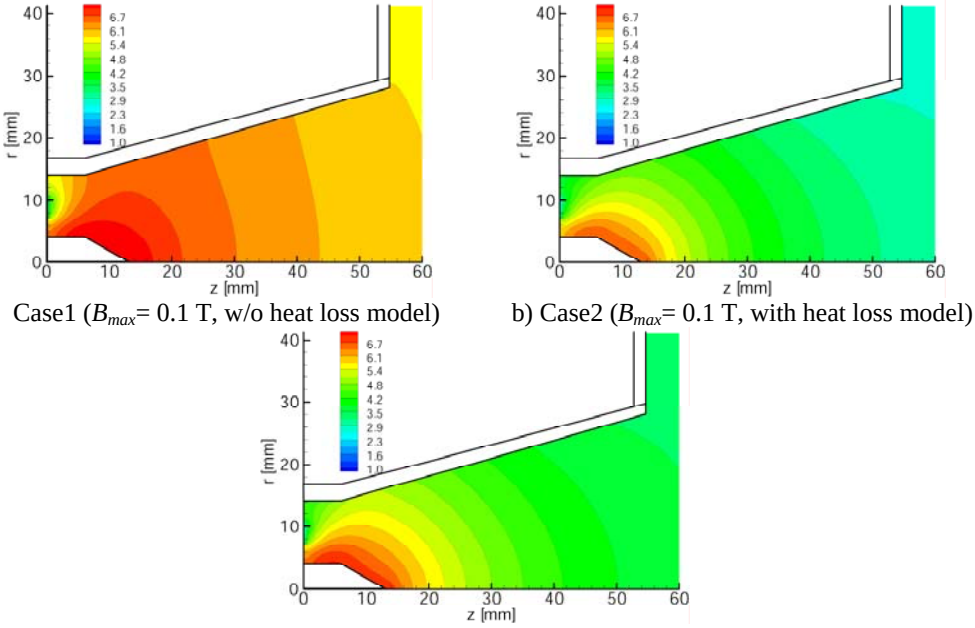

a) Case1 (B_{max}= 0.1 T, w/o heat loss model) b) Case2 (B_{max}= 0.1 T, with heat loss model)

c) Case3 (B_{max}= 0.15 T, with heat loss model)

Figure 6. Electron temperature, eV, Ar, 0.1 g/s, *J* = 1 kA.

Table 4 Heat loss on anode surface.

	Case2 (B_{max}=0.1 T)	Case3 (B_{max}=0.15 T)
Q_{ent} [kW]	7.44	8.27
Q_{conv} [kW]	14.9	16.8
Q_{sh} [kW]	15.3	17.1
Q_p [kW]	22.3	25.1
Q_a [kW]	6.97	7.96
Q_p/P_{net}	0.549	0.477
Q_a/P_{net}	0.172	0.151

E. Energy conversion process

To attain high thrust efficiency, an input power has to be converted into an axial kinetic energy efficiently. Here, the influences of the calculation conditions on the energy flux of the axial kinetic energy. The energy flux of the axial kinetic energy E_k is defined as

$$E_k = \int \frac{1}{2} \rho u^2 u dS_z \tag{35}$$

where u represents the axial component of the velocity vector. Figure 7 shows the axial distribution of E_k. In all cases, E_k has almost the same value between the inlet and the cathode tip ($0 < z < 13$ mm), but there appears some difference in the downstream region. The decrease in E_k seen in the plume region is related with radial leak of plasma from the computational domain.

In Case1, the significant aerodynamic acceleration attributed to the boundary condition of $\nabla T_e = 0$ yields the highest E_k at the outlet (z = 55 mm). In Case2, the heat loss of electron energy degrades the aerodynamic acceleration, which results in the decrease in E_k within the thruster. It is noted that the E_k for Case3 is less than that for Case2 within the thruster, but this relation becomes opposite in the plume region. This can be also seen from the axial velocity distribution shown in Fig. 8. The axial velocity within the thruster for Case3 is less than that of Case2, and is rapidly increased in the plume region. This will be due to the effect of the magnetic nozzle enhanced by the increase in the applied magnetic field of Case3, i.e. the stronger applied magnetic field prevents the plasma from efficient aerodynamic acceleration within the thruster. As the magnetic field diverges in the plume region, the thermally deposited energy is aerodynamically and electromagnetically accelerated.

The azimuthal velocity distribution is shown in Fig. 9. The flow is mainly accelerated in the azimuthal direction around the cathode up to about 10 km/s. This swirl motion produces centrifugal force leading to an increase in the pressure as shown in Fig.10. In Case2, there is a low pressure region near the symmetric axis owing to the centrifugal force, while this tendency is moderated in Case3 due to the higher magnetic pressure confining the plasma. This confining effect will contribute to the reduction of the heat loss on the anode surface.

IV. Conclusion

Numerical simulation on the energy conversion processes in an applied magnetoplasmadynamic thruster has been conducted with argon propellant of 0.1 g/s for a discharge current of 1 kA and an applied magnetic field of 0.1-0.15 T. An anode sheath model is taken into account, which enables to quantitatively estimate an anode heat loss. With the sheath model, around the outlet of the thruster, the sheath effect makes the current contour lines shifted toward upstream region. Then about 50% of the net power input into the plasma is lost to the anode surface, whereas the actual heat loss transferred to the anode is reduced to 15-17% of the net input power due to the presence of an ion-rich sheath. An increase in the strength of the applied magnetic field enhances confinement of the plasma, which results in reduction of the anode heat loss.

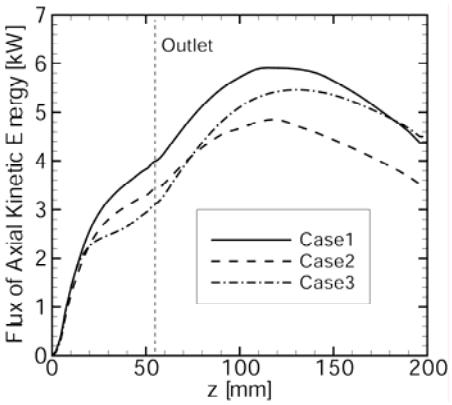

Figure 7. Energy flux of axial kinetic energy, Ar, 0.1g/s, *J* = 1 kA.

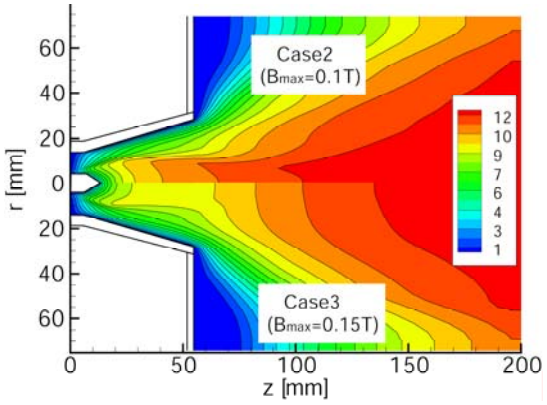

Figure 8. Axial velocity distribution, km/s, Ar, 0.1g/s, *J* = 1 kA.

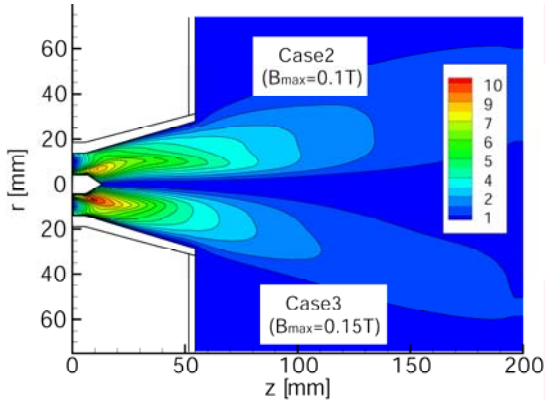

Figure 9. Azimuthal velocity distribution (absolute value), km/s, Ar, 0.1g/s, *J* = 1 kA.

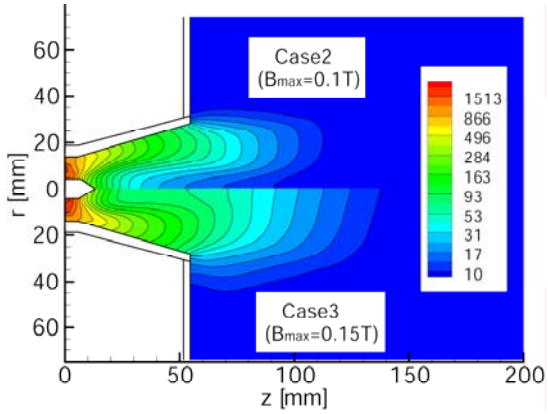

Figure 10. Pressure distribution, Pa, Ar, 0.1g/s, *J* = 1 kA.

Acknowledgments

This work was supported by Grant-in-Aid for Scientific Research （20·9404）. We appreciate JAXA's Engineering Digital Innovation Center.

References

[1]Krülle, G., Auweter-Kurtz, M., Sasoh, A., "Technology and Application Aspects of Applied Field Magnetoplasmadynamic Propulsion," *Journal of Propulsion and Power*, Vol. 14, No. 5, 1998, pp.754-763.

[2]Kodys, A. D., and Choueiri, E. Y., "A Critical Review of the State-of-the-Art in the Performance of Applied-field Magnetoplasmadynamic Thrusters," AIAA Paper 2005-4247, 2005.

[3]Tanaka, M., and Kimura, I., "Current Distribution and Plasma Acceleration in MPD Arcjets with Applied Magnetic Fields," *Journal of Propulsion and Power*, Vol. 4, No. 5, 1988, pp.428-436.

[4]Thomas, H., Chapman, R. and Garrison, G. W., "A Numerical Simulation of Axisymmetric Steady-State Plasma Flow Through MPD-Type Thrusters with Applied Magnetic Fields," AIAA paper 92-3737, 1992.

[5]Mikellides, P. G., Turchi, P. J., and Roderick, N. F., "Applied-Field Magnetoplasmadynamic Thruters, Part 1: Numerical Simulations Using the MACH2 Code," *J. Propul. Power*, Vol. 16, No. 5, 2000, pp.887-893.

[6]Haag, D., Fertig, M., and Auweter-Kurtz, M., "Numerical Simulations of Magnetoplasmadynamic Thrusters with Coaxial Applied Magnetic Field," 30th International Electric Propulsion Conference, IEPC-2007-138, 2007.

[7]Myers, R. M., "Geometric Scaling of Applied-Field Magnetoplasmadynamic Thrusters," *J. Propul. Power*, Vol. 11, No. 2, 1995, pp. 343-350.

[8]Mikellides, P. G., "Modeling and Analysis of a Megawatt-Class Magnetoplasmadynamic Thruster," *J. Propul. Power*, Vol. 20, No. 2, 2004, pp. 204-210.
[9]Roy, S., "Self Consistent Electrode Model for Magnetoplasmadynamic Thrusters," AIAA paper 2004-3469, 2004.
[10]Niewood, E. H., and Martinez-Sanchez, M., "An Explanation for Anode Voltage Drops in MPD Thrusters," AIAA paper 93-2104, 1993.
[11]Schade, E., and Shmelev, D. L., "Numrical Simulation of High-Current Vacuum Arcs With an External Axial Magnetic Field," *IEEE Trans. Plasma Sci.*, Vol. 31, No. 5, 2003, pp. 890-901.
[12]Lotz, W., "Electron-Impact Ionzation Cross-Sections and Ionization Rate Coefficients for Atoms and Ions from Hydrogen to Calcium," *Zeitschrift für Physik*, Vol. 216, 1968, pp. 241-247.
[13]Mitchner, M., and Kruger, C. H., *Partially Ionized Gases*, John Wiley & Sons, 1973.
[14]Sutton, G. W., and Sherman, A., *Engineering Magnetohydrodynamics*, Dover Publications, 2006.
[15]Boie, C., Auweter-Kurtz, M., Kaeppeler, H. J., and Sleziona, P. C., "Numerical Investigation of MPD Thrusters with Unstructured Mesh Methods," 24th International Electric Propulsion Conf., Paper IEPC-95-168, Sept. 1995.
[16]Lieberman, M. A, and Lichtenberg, A. J., *Principles of Plasma Discharges and Materials Processing*, 2nd ed., John Wiley & Sons, 2005.
[17]Fujita, K., "Arc Column Behavior and Heat Loss Mechanism in a DC Arcjet Thruster," Ph.D. Dissertation, Univ. of Tokyo, 1994.
[18]Tóth, G., and Odstrõil, D., "Comparison of Some Flux Corrected Transport and Total Variation Diminishing Numerical Schemes for Hydrodynamic and Magnetohydrodynamic Problems," *J. Comput. Phys.*, Vol. 128, 1996, pp. 82-100.
[19]Fujita, K., and Arakawa, Y., "Performance Computation of a Low-Power Hydrogen Arcjet," *J. Propul. Power*, Vol. 15, No. 1, 1999, pp. 144-150.
[20]Tahara, H., "Arc Structure in a Quasi-Steady MPD Thruster," ***J.*** *Jpn. Soc. Aeronaut. Space Sci.*, Vol. 33, No. 382, 1985, pp. 42-50 (in Japanese).